



Aging behavior of two refractory Ti-Nb-(Hf, Zr)-Al high entropy alloys

E. Panina*, N. Yurchenko, S. Zherebtsov, N. Stepanov

Laboratory of Bulk Nanostructured Materials, Belgorod State University, Belgorod 308015, Russia



ARTICLE INFO

Article history:

Received 11 June 2021

Received in revised form 31 July 2021

Accepted 12 August 2021

Available online 14 August 2021

Keywords:

Refractory high entropy alloys

Microstructure

Phase transformations

CALPHAD

Precipitation hardening

ABSTRACT

In the present study, the response of $\text{Ti}_{40}\text{Nb}_{30}\text{Hf}_{15}\text{Al}_{15}$ and $\text{Ti}_{40}\text{Nb}_{30}\text{Zr}_{20}\text{Al}_{10}$ (at%) refractory high entropy alloys to annealing is reported. The alloys were produced by vacuum arc melting and had a density of $7.07 \pm 0.03 \text{ g/cm}^3$ and $6.03 \pm 0.03 \text{ g/cm}^3$, respectively. In the as-cast condition, both alloys had a coarse-grained single B2 phase structure. After cold rolling to 80% thickness reduction and annealing at $T = 900 \text{ }^\circ\text{C}$ for 15 min, a fine-grained structure with a grain size of 4.3 ± 2.2 and $13.2 \pm 5.0 \text{ }\mu\text{m}$ was produced in the $\text{Ti}_{40}\text{Nb}_{30}\text{Hf}_{15}\text{Al}_{15}$ and $\text{Ti}_{40}\text{Nb}_{30}\text{Zr}_{20}\text{Al}_{10}$ alloys, respectively. In addition, a small amount of orthorhombic (O) and Zr_5Al_3 -type phase particles formed in the alloys with Hf and Zr, respectively. Annealing at $T = 500 \text{ }^\circ\text{C}$ up to 96 h had a weak effect on the structure and hardness of the alloys. Annealing at $T = 600$ and $T = 700 \text{ }^\circ\text{C}$ resulted in the massive precipitation of the O-phase in the $\text{Ti}_{40}\text{Nb}_{30}\text{Hf}_{15}\text{Al}_{15}$ alloy and the Zr_5Al_3 -type phase in the $\text{Ti}_{40}\text{Nb}_{30}\text{Zr}_{20}\text{Al}_{10}$ alloy. However, a pronounced increase in microhardness of the $\text{Ti}_{40}\text{Nb}_{30}\text{Hf}_{15}\text{Al}_{15}$ alloy was revealed after annealing at $T = 600 \text{ }^\circ\text{C}$ only. Meanwhile, the $\text{Ti}_{40}\text{Nb}_{30}\text{Zr}_{20}\text{Al}_{10}$ alloy became softer after annealing at $T = 600$ and $T = 700 \text{ }^\circ\text{C}$. The phase transformations in the alloys were compared with the CALPHAD predictions, and hardening mechanisms were qualitatively analyzed.

© 2021 Elsevier B.V. All rights reserved.

1. Introduction

There is an urgent need for new metallic materials to withstand high temperatures in the aerospace and energy industries [1]. A new class of promising refractory alloys has recently appeared – refractory high-entropy alloys (RHEAs) [2–18]. These alloys typically have bcc solid solution structures with the possible presence of other phases, including B2, Laves and/or different compounds [8,10,19,20]. RHEAs often exhibit high strength at elevated temperatures, making them promising materials for high-temperature applications [3,8,21–23]. However, most RHEAs have low ductility at room temperature, even in compression [3,24–27].

The vast experience from conventional alloys suggests that a better balance between high-temperature strength, ambient temperature ductility, and damage tolerance can be obtained in precipitation-hardened alloys. A famous example is Ni-based superalloys, where a Ni-based fcc matrix is strengthened by ordered L_{12} Ni_3Al precipitates [28,29]. There were extensive efforts to replicate that kind of microstructure in RHEAs, resulting in developing the so-called refractory high entropy superalloys (RHESAs) [30–36]. RHESAs are usually composed of coherent bcc and B2 phases having cuboidal and/or plate-like morphology and can demonstrate

impressive specific strength at elevated temperatures. For example, an $\text{AlMo}_{0.5}\text{NbTa}_{0.5}\text{TiZr}$ alloy has a density of 7.4 g/cm^3 and yield strength of 745 MPa at 1273 K [37].

However, in most RHESAs, the matrix phase has a B2 ordered structure, which results in a lack of room-temperature ductility [37,38]. Indeed, for the $\text{Al}_{0.5}\text{NbTa}_{0.8}\text{Ti}_{1.5}\text{V}_{0.2}\text{Zr}$ alloy, it was demonstrated that proper heat treatment could “reverse” microstructure and improve ductility [39]. Yet, it is unclear if these approaches are universal and suitable for different RHESAs. In addition, some recent works have raised doubts about the stability of bcc+B2 structures at potential usage temperatures [40,41].

Therefore, there is an interest in other approaches to develop precipitation-strengthened RHEAs. Recently, several new RHEAs with an orthorhombic (O) phase embedded in the bcc matrix were introduced [42,43]. For example, in a $\text{Ti}_{40}\text{Nb}_{30}\text{Hf}_{15}\text{Al}_{15}$ alloy [42], the O-phase increased strength with a slight decrease in plasticity.

However, additional knowledge about the O-phase precipitation in RHEAs is needed. One of the interesting aspects is related to the effect of heat treatment (i.e., aging) on characteristics of the O-phase precipitation. Another one is associated with the compositional effect on the O-phase formation. In this work, we have performed a detailed examination of the effect of aging conditions on the previously reported $\text{Ti}_{40}\text{Nb}_{30}\text{Hf}_{15}\text{Al}_{15}$ alloy. In addition, similar studies were conducted for a novel $\text{Ti}_{40}\text{Nb}_{30}\text{Zr}_{20}\text{Al}_{10}$ alloy, where Hf was

* Corresponding author.

E-mail address: panina_e@bsu.edu.ru (E. Panina).

Table 1

Measured chemical compositions of the $\text{Ti}_{40}\text{Nb}_{30}\text{Hf}_{15}\text{Al}_{15}$ and $\text{Ti}_{40}\text{Nb}_{30}\text{Zr}_{20}\text{Al}_{10}$ alloys, in at%.

Alloy	Ti	Nb	Hf	Zr	Al	O, ppm	N, ppm
$\text{Ti}_{40}\text{Nb}_{30}\text{Hf}_{15}\text{Al}_{15}$	42.8	28.8	15.2	–	13.2	401	83
$\text{Ti}_{40}\text{Nb}_{30}\text{Zr}_{20}\text{Al}_{10}$	41.2	28.6	–	20.1	10.2	227	43

replaced with chemically similar (same group in the periodic table) yet lighter Zr.

2. Materials and methods

Ingots of the $\text{Ti}_{40}\text{Nb}_{30}\text{Hf}_{15}\text{Al}_{15}$ and $\text{Ti}_{40}\text{Nb}_{30}\text{Zr}_{20}\text{Al}_{10}$ (in at%) alloys with dimensions of $10 \times 15 \times 40 \text{ mm}^3$ were produced by vacuum arc melting of pure ($\geq 99.9 \text{ wt}\%$) elements in a high purity argon atmosphere; the actual chemical composition, measured with an energy-dispersive (EDX) detector (for principal components) and inert gas fusion (for oxygen and nitrogen contents), is listed in Table 1. The densities of the $\text{Ti}_{40}\text{Nb}_{30}\text{Hf}_{15}\text{Al}_{15}$ and $\text{Ti}_{40}\text{Nb}_{30}\text{Zr}_{20}\text{Al}_{10}$ alloys, determined by the hydrostatic weighing method, were $7.07 \pm 0.03 \text{ g/cm}^3$ and $6.03 \pm 0.03 \text{ g/cm}^3$, respectively.

The obtained ingots were rolled at room temperature until the thickness was reduced by 80%. Although the B2-phase is considered brittle, in our case the alloys withstood cold rolling without noticeable cracking. Similarly, some B2 compounds have been reported to be ductile during rolling or compression at ambient temperatures in [42,44–47]. Rectangular samples measured $3 \times 4 \times 1 \text{ mm}^3$ were cut from the cold-rolled ingots. The samples were encapsulated in vacuumed (10^{-2} Torr) quartz ampules filled with titanium chips to prevent oxidation. All samples were annealed at $T = 900 \text{ }^\circ\text{C}$ for 15 min. These samples will be referred to as “recrystallized” hereinafter. Some samples were further annealed at $T = 500, 600,$ and $700 \text{ }^\circ\text{C}$ for 1, 12, 24, 48, 96 h. These samples will be denoted as “aged” hereafter. Cooling after the annealing was carried out in laboratory air. Vickers microhardness was measured at room temperature using a 300 g load for 15 s; 15 measurements were made for each specimen.

The phase composition and microstructure of the alloys in the as-cast, recrystallized, and aged conditions were studied using X-ray diffraction (XRD), scanning electron microscopy (SEM), and transmission electron microscopy (TEM). Samples for SEM and XRD analysis were prepared by careful mechanical polishing. XRD analysis was performed using a RIGAKU diffractometer and $\text{Cu K}\alpha$ radiation having the wavelength of 1.5406 \AA and a scanning rate of $3^\circ/\text{min}$ from 20° to 125° . SEM investigations were carried out on an FEI Quanta 600 FEG or Nova NanoSEM 450 microscopes equipped with an EDX detector; the latter was used for the chemical composition measurements. Mechanically pre-thinned to $100 \text{ }\mu\text{m}$ foils were prepared for TEM analysis by conventional twin-jet electro-polishing at a temperature of $-35 \text{ }^\circ\text{C}$ and an applied voltage of 29.5 V in a mixture of 600 ml of methanol, 360 ml of butanol, and 60 ml of perchloric acid. TEM investigations were performed using a JEOL JEM-2100 microscope equipped with an EDS detector.

Dependences of the equilibrium phases fraction on temperature in the program alloys were constructed using a Thermo-Calc (version 2020a) software and a TCHEA4 (high-entropy alloys) database.

3. Results

3.1. Microstructure in the as-cast and recrystallized conditions

Fig. 1 illustrates microstructures of the $\text{Ti}_{40}\text{Nb}_{30}\text{Hf}_{15}\text{Al}_{15}$ and $\text{Ti}_{40}\text{Nb}_{30}\text{Zr}_{20}\text{Al}_{10}$ alloys in the as-cast condition. The alloys had a

single-phase B2 structure with the lattice parameter $a = 0.3304 \text{ nm}$ and 0.3337 nm , respectively (Fig. 1a). The average grain size was 470 ± 150 (Fig. 1b) and $445 \pm 190 \text{ }\mu\text{m}$ (Fig. 1c), respectively. Dendritic segregations were observed inside the grains of the $\text{Ti}_{40}\text{Nb}_{30}\text{Zr}_{20}\text{Al}_{10}$ alloy. Comparison between the SEM-BSE image and EDX element maps (Fig. 1c) shows that darker areas were enriched with Zr and Al, while lighter regions were enriched with Nb. The $\text{Ti}_{40}\text{Nb}_{30}\text{Hf}_{15}\text{Al}_{15}$ alloy had a uniform chemical composition.

A uniform fine-grained recrystallized microstructure was obtained in both alloys after cold rolling to 80% reduction and annealing at $900 \text{ }^\circ\text{C}$ for 15 min (Fig. 2a and c). The average grain size was 4.3 ± 2.2 and $13.2 \pm 5.0 \text{ }\mu\text{m}$ in the $\text{Ti}_{40}\text{Nb}_{30}\text{Hf}_{15}\text{Al}_{15}$ (Fig. 2a) and $\text{Ti}_{40}\text{Nb}_{30}\text{Zr}_{20}\text{Al}_{10}$ (Fig. 2c) alloys, respectively. In both alloys, the precipitation of secondary phases was detected (Fig. 2b and c). Using TEM, the particles were identified as a disordered O1-phase in $\text{Ti}_{40}\text{Nb}_{30}\text{Hf}_{15}\text{Al}_{15}$ (Fig. 2b) and a Zr_5Al_3 -type (hcp) phase in $\text{Ti}_{40}\text{Nb}_{30}\text{Zr}_{20}\text{Al}_{10}$ (Fig. 2d). According to EDS analysis, the O1-phase was enriched with Hf, while the Zr_5Al_3 -type phase was enriched with Zr and Al (Table 2). The O1 particles were distributed homogeneously in the microstructure of the $\text{Ti}_{40}\text{Nb}_{30}\text{Hf}_{15}\text{Al}_{15}$ alloy. The estimated volume fraction of the O1 particles and their average size were $\sim 1.5\%$ and 25 nm , respectively. In the case of the $\text{Ti}_{40}\text{Nb}_{30}\text{Zr}_{20}\text{Al}_{10}$ alloy, the Zr_5Al_3 -type particles were mainly observed in darker, Zr-, Al-rich areas (Fig. 2c). The volume fraction and average size of the Zr_5Al_3 -type particles were 1.2% and 325 nm , respectively.

3.2. Effect of aging conditions on microhardness

The $\text{Ti}_{40}\text{Nb}_{30}\text{Hf}_{15}\text{Al}_{15}$ alloy in the recrystallized condition (after rolling to 80% reduction and annealing at $900 \text{ }^\circ\text{C}$ for 15 min) had a microhardness of $340 \pm 20 \text{ HV}$ (Fig. 3a). The $\text{Ti}_{40}\text{Nb}_{30}\text{Zr}_{20}\text{Al}_{10}$ alloy in the recrystallized condition had a slightly lower microhardness of $305 \pm 5 \text{ HV}$ (Fig. 3b), probably due to somewhat coarser grain size and/or different chemical composition (Fig. 2a and c). Aging at $500 \text{ }^\circ\text{C}$ had barely affected the microhardness of the $\text{Ti}_{40}\text{Nb}_{30}\text{Hf}_{15}\text{Al}_{15}$ alloy. Aging for 1–12 h at $600 \text{ }^\circ\text{C}$ also resulted in a weak increase in hardness. However, an increase in the aging duration to 24 h resulted in a sharp rise in hardness to $430 \pm 10 \text{ HV}$, which remained constant at longer aging durations. A slight increase in the microhardness values was found after aging at $700 \text{ }^\circ\text{C}$.

The $\text{Ti}_{40}\text{Nb}_{30}\text{Zr}_{20}\text{Al}_{10}$ alloy exhibited a very different behavior during aging treatment. Some variations in the hardness during aging treatment at $500 \text{ }^\circ\text{C}$ were detected, yet it still was not significantly different from the hardness of the recrystallized condition. Meanwhile, aging at higher temperatures of 600 and $700 \text{ }^\circ\text{C}$ resulted in a continuous decrease in hardness with increasing duration of heat treatment. The hardness reached $290 \pm 5 \text{ HV}$ and $285 \pm 5 \text{ HV}$ after aging for 96 h at 600 and $700 \text{ }^\circ\text{C}$, respectively.

3.3. Effect of aging on structure

3.3.1. The $\text{Ti}_{40}\text{Nb}_{30}\text{Hf}_{15}\text{Al}_{15}$ alloy

To examine the aging effect on the structure of the $\text{Ti}_{40}\text{Nb}_{30}\text{Hf}_{15}\text{Al}_{15}$ alloy, XRD analysis was performed first. The recrystallized $\text{Ti}_{40}\text{Nb}_{30}\text{Hf}_{15}\text{Al}_{15}$ alloy had the B2 structure; reflections from the disordered O1-phase were not detected, probably due to their low fraction (Fig. 2b). Aging at $500 \text{ }^\circ\text{C}$ did not result in noticeable changes in the phase composition (Fig. 4a). Aging at $600 \text{ }^\circ\text{C}$ for 1–12 h did also not result in any changes (Fig. 4b). However, after aging for 24–96 h, strong peaks belonging to a new ordered O2-phase appeared. The precipitation of the new phase was also accompanied by shifting of the B2 peaks to the left, indicating some decrease in the lattice parameter. Similar behavior was observed

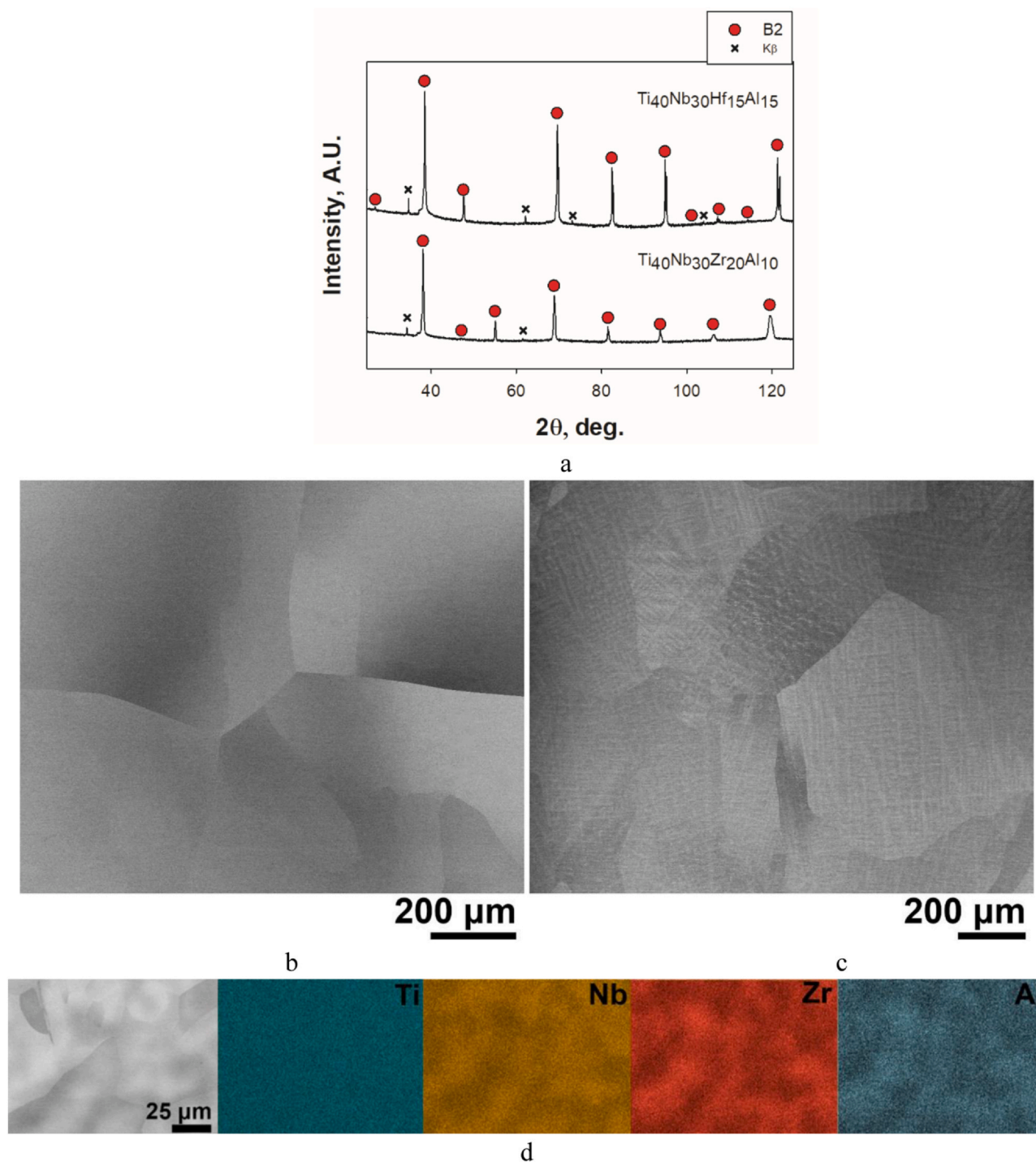


Fig. 1. XRD pattern (a) and SEM-BSE images of the $\text{Ti}_{40}\text{Nb}_{30}\text{Hf}_{15}\text{Al}_{15}$ (b) and $\text{Ti}_{40}\text{Nb}_{30}\text{Zr}_{20}\text{Al}_{10}$ (c) alloys microstructure in the as-cast state; EDX element maps of the $\text{Ti}_{40}\text{Nb}_{30}\text{Zr}_{20}\text{Al}_{10}$ alloy.

during aging at 700 °C (Fig. 4c). The recrystallized structure was stable during short-time (1 h) aging; however, an increase in the aging duration caused the O2-phase precipitation and shift of the B2 peaks to the left.

To get a better understanding of the structural response to aging, we performed SEM and TEM analysis. Fig. 5 demonstrates the effect of aging at $T = 500$ (a, b), 600 (c, d), 700 °C (e, f) for 24 h on the microstructure of the $\text{Ti}_{40}\text{Nb}_{30}\text{Hf}_{15}\text{Al}_{15}$ alloy. Table 3 summarizes the

chemical composition and average size of the structural constituents. Aging at 500 °C barely changed the recrystallized microstructure and chemical composition of the B2 and O1-phases (Fig. 5a, b, g; Table 3).

However, at $T = 600$ °C and 700 °C, needle-shaped particles of the ordered O2-phase precipitated in the B2 matrix after aging for 24 h (Fig. 5c–f), confirming the XRD results (Fig. 4b). Note, both the O2-phase particles' size and volume fraction were smaller at 600 °C

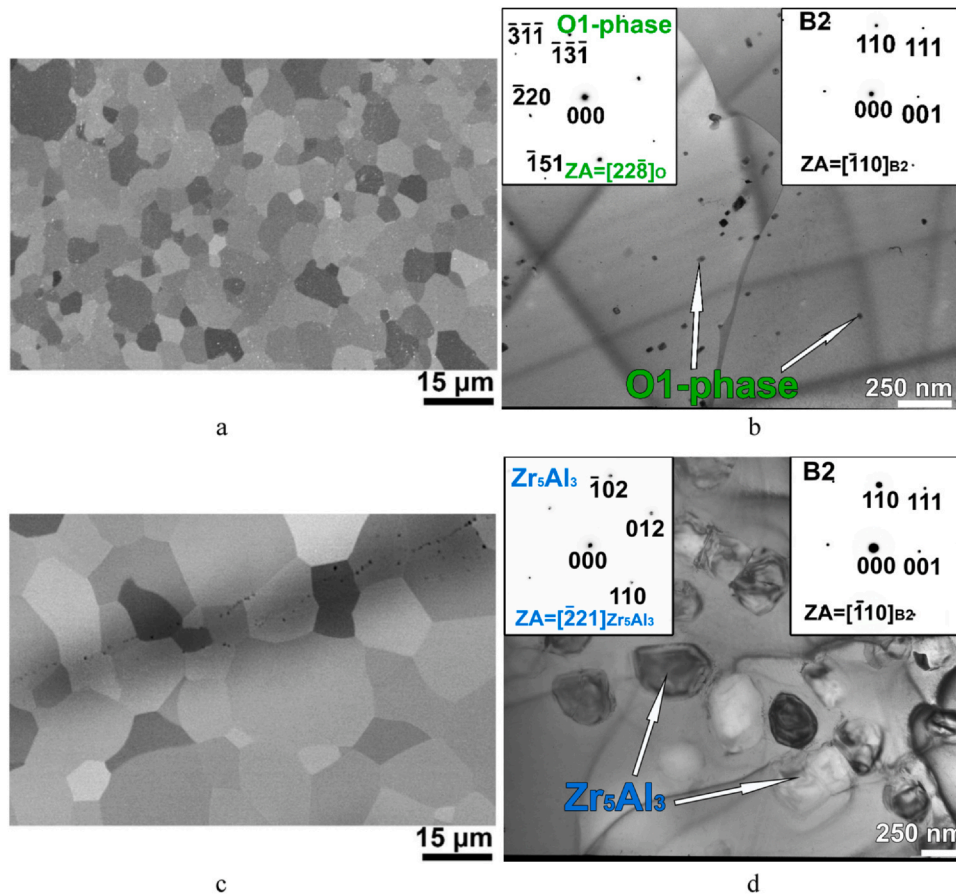


Fig. 2. Microstructure of the $\text{Ti}_{40}\text{Nb}_{30}\text{Hf}_{15}\text{Al}_{15}$ (a, b) and $\text{Ti}_{40}\text{Nb}_{30}\text{Zr}_{20}\text{Al}_{10}$ (c, d) alloys in the recrystallized condition: a, c – SEM-BSE images; b, d – TEM bright-field images with selected area diffraction patterns (SAEDs) of the B2 and O1-phases (b) and the B2 and Zr_5Al_3 -type phases (d).

(Fig. 5g; Table 3). Meanwhile, the precipitation kinetics at 600 and 700 °C were found to be similar (Fig. 5g). After a certain period (24 h for 600 °C and 12 h for 700 °C), the particles' volume fraction steeply increased and remained almost constant during further aging. Besides, the EDS analysis revealed similarities of the chemical compositions of the B2 and O2-phases after aging at 600 and 700 °C. The B2 phase was enriched with Nb and Hf, while the O2-phase – with Ti and Al (Table 3). The B2 and O2-phases also demonstrated the following orientation relationships (ORs): $[01\bar{1}]_{\text{B2}}||[00\bar{1}]_{\text{O2}}$, $(\bar{2}11)_{\text{B2}}||(\bar{1}10)_{\text{O2}}$ (Fig. 5d) and $[111]_{\text{B2}}||[110]_{\text{O2}}$, $(110)_{\text{B2}}||(\text{O}01)_{\text{O2}}$, (Fig. 5f).

3.3.2. The $\text{Ti}_{40}\text{Nb}_{30}\text{Zr}_{20}\text{Al}_{10}$ alloy

The XRD patterns of the $\text{Ti}_{40}\text{Nb}_{30}\text{Zr}_{20}\text{Al}_{10}$ alloy in the recrystallized condition and after aging at 500 (a), 600 (b), 700 °C (c) are presented in Fig. 6. The recrystallized $\text{Ti}_{40}\text{Nb}_{30}\text{Zr}_{20}\text{Al}_{10}$ alloy

comprised of the B2 and Zr_5Al_3 -type (hcp) phases. The Bragg peaks belonging to the Zr_5Al_3 -type phase became more intense with increasing aging duration at 500–700 °C, suggesting some increment in its volume fraction.

Fig. 7 demonstrates the effect of aging at $T = 500$ (a, b), 600 (c, d), 700 °C (e, f) on the microstructure of the $\text{Ti}_{40}\text{Nb}_{30}\text{Zr}_{20}\text{Al}_{10}$ alloy. Table 4 collects data on the chemical compositions and volume fractions of the constitutive phases. After aging at $T = 500$ °C for 24 h, the structure remained unchanged (Fig. 2a and b). The Zr_5Al_3 -type particles were found in darker areas enriched with Zr and Al. However, an increase in the aging duration to 48–96 h enlarged the volume fraction of the Zr_5Al_3 -type particles to 5–15% (Fig. 7g).

After aging at 600 and 700 °C for 24 h, the Zr_5Al_3 -type particles appeared both in the B2 grain interior and at the boundaries (Fig. 7c–f). Compared to 600 °C, a twice higher volume fraction of much coarser Zr_5Al_3 -type particles was found at 700 °C (Table 4).

Table 2

Measured chemical composition of structural constituents in the $\text{Ti}_{40}\text{Nb}_{30}\text{Hf}_{15}\text{Al}_{15}$ and $\text{Ti}_{40}\text{Nb}_{30}\text{Zr}_{20}\text{Al}_{10}$ alloys in the recrystallized condition.

Alloy	Phase	Fraction, %	Chemical composition, at%				
			Ti	Nb	Hf	Zr	Al
$\text{Ti}_{40}\text{Nb}_{30}\text{Hf}_{15}\text{Al}_{15}$	B2	98.5	43.1	29.2	14.5	–	13.2
	O1-phase	1.5	29.1	19.8	51.1	–	0.0
	Nominal	–	42.8	28.8	15.2	–	13.2
$\text{Ti}_{40}\text{Nb}_{30}\text{Zr}_{20}\text{Al}_{10}$	B2	98.8	41.4	30.6	–	19.6	8.4
	Zr_5Al_3	1.2	12.8	10.2	–	39.7	37.3
	Nominal	–	41.2	28.6	–	20.1	10.2

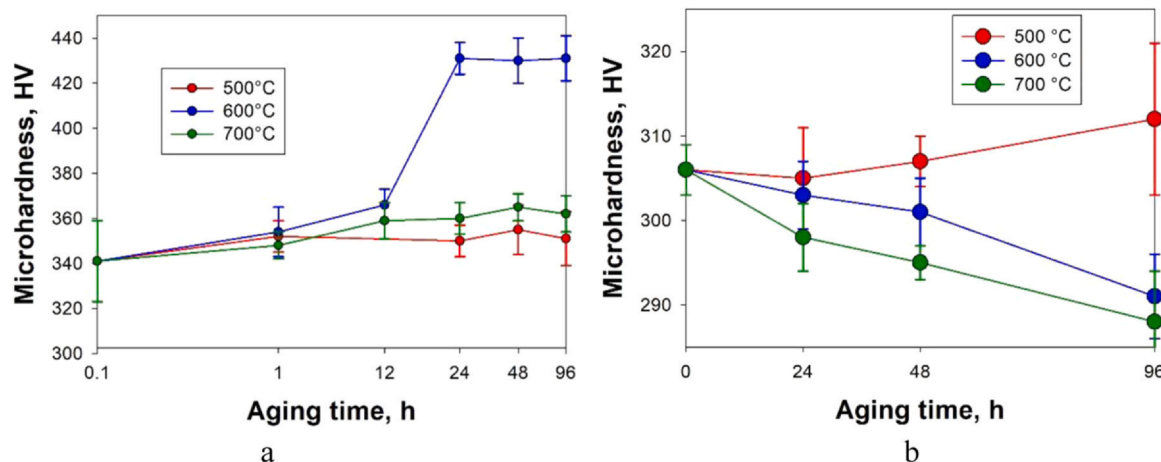


Fig. 3. Microhardness of the Ti₄₀Nb₃₀Hf₁₅Al₁₅ (a) and Ti₄₀Nb₃₀Zr₂₀Al₁₀ (b) alloys in the recrystallized condition and after subsequent aging at different conditions.

Meanwhile, an increase in the aging duration to 96 h rose the volume fraction of the Zr₅Al₃-type phase to 23% and 19% at 600 and 700 °C, respectively (Fig. 7g). The average particle size also increased to 1.4 μm and 2.1 μm at 600 and 700 °C, respectively.

4. Discussion

In the present study, structure and microhardness of Ti₄₀Nb₃₀Hf₁₅Al₁₅ and Ti₄₀Nb₃₀Zr₂₀Al₁₀ RHEAs in different conditions (as-cast, cold-rolled, and annealed at 900 °C (recrystallized), annealed further at 500–700 °C (aged)) were examined. Although the structure and hardness of both alloys were relatively similar in the as-cast and recrystallized conditions, the microstructural response to aging was drastically different. Here, we analyze the difference in the behavior of the Ti₄₀Nb₃₀Hf₁₅Al₁₅ and Ti₄₀Nb₃₀Zr₂₀Al₁₀ alloys.

While both alloys had the B2 ordered matrix, the replacement of Hf with Zr produced different secondary phases. In the Ti₄₀Nb₃₀Hf₁₅Al₁₅ alloy, a small amount of the disordered O1-phase was found after cold rolling and recrystallization annealing. This O1-phase was retained after aging at 500 °C, while aging at 600 and 700 °C resulted in the massive precipitation of the ordered O2-phase. In turn, the recrystallized Ti₄₀Nb₃₀Zr₂₀Al₁₀ alloy contained a small amount of the Zr₅Al₃-type particles, and aging at 500–700 °C led to a pronounced increase in the fraction of this phase. To rationalize these findings, we constructed equilibrium phase diagrams using the CALPHAD (CALculation of PHase Diagrams) method (Fig. 8).

According to the produced phase diagram, the Ti₄₀Nb₃₀Hf₁₅Al₁₅ alloy crystallizes through the bcc phase in a temperature range of 1600–1780 °C (Fig. 8a). The alloy has a single bcc phase structure till ≈900 °C. At lower temperatures, the formation of the ordered O2-phase and hcp phase is expected. The solvus temperatures of the O2-phase and hcp phase are ≈900 and ≈795 °C, respectively. The O2-phase is composed of Ti and Al. In turn, the hcp phase is enriched with Zr and Al (Table 5).

The Ti₄₀Nb₃₀Zr₂₀Al₁₀ alloy has similar liquidus and solidus temperatures of 1790 and 1697 °C, respectively (Fig. 8b). A broad single bcc phase field ends at a temperature of 940 °C due to the Zr₅Al₃ phase formation. The Zr₅Al₃ phase is replaced with an AlZr₂ phase at ≈830 °C. In addition, a second bcc phase (denoted as “bcc₂” in Fig. 8b) appeared at ≈570 °C. The Zr₅Al₃/Zr₂Al phases had close to stoichiometric compositions, while the bcc₂ phase was enriched with Nb.

A reasonable correlation between the predicted phase diagrams and the experimental results is observed. For instance, the prognosticated bcc-based matrix in both alloys and the type of the precipitating phases – O phase in the Ti₄₀Nb₃₀Hf₁₅Al₁₅ alloy and Zr aluminide in the Ti₄₀Nb₃₀Zr₂₀Al₁₀ alloy – were indeed found. The solvus temperature of the secondary phases of ≈900/940 °C in Hf/Zr-containing alloys agrees fairly with the experimental observation of a small fraction of these phases after recrystallization annealing at 900 °C (Fig. 2). Note that the particles in the recrystallized conditions can be formed during cooling after annealing as no specific attention was paid to ensure fast cooling rates. The CALPHAD method thus confirms the negative influence of Zr on the O-phase stabilization, which is also in agreement with some recent results [43]. The effect of Zr can be associated with a highly negative enthalpy of the Zr aluminides formation [48], making their appearance preferable over the Ti₂AlNb-based O-phase.

Some discrepancies between the experimental data and CALPHAD results must also be mentioned. For example, the B2 ordering of the matrix phase in both alloys was not predicted. The absence of an adequate B2 phase description in refractory metals containing binaries and ternaries and available CALPHAD databases are the apparent reasons for that inconsistency [30,49]. The predicted phase transformations at low temperatures, like the hcp phase formation in the Hf-containing alloy and the Zr₅Al₃ to AlZr₂ transition coupled with the second bcc phase precipitation in the Zr-containing alloy, can be incorrect due to similar reasons. Yet, the obtained results suggest very sluggish diffusion in both alloys at 600 °C due to the absence of any noticeable changes in structure even after 96 h of aging. Longer aging durations must be needed to produce equilibrium structures at this temperature. This task, however, is beyond the scope of the present work.

Another interesting finding is appearing two variants of the O-phase in the Ti₄₀Nb₃₀Hf₁₅Al₁₅ alloy – O1 and O2-phases. Although the presence of the O1- and O2-phases is typical for the Ti₂AlNb alloys [50,51], the relationship between them is still controversial due to lacking experimental data. Muraleedharan et al. [50] proposed that the high-temperature, disordered O1-phase transforms to the low-temperature, ordered O2-phase by changing atomic site occupation. An additional suggestion for the O1/O2-phase existence was that Al could stabilize the martensitic orthorhombic phase in the Ti-Nb system [50,51]. Our results showed that, despite the crystal lattice similarity, the O1-phase has a very different chemical

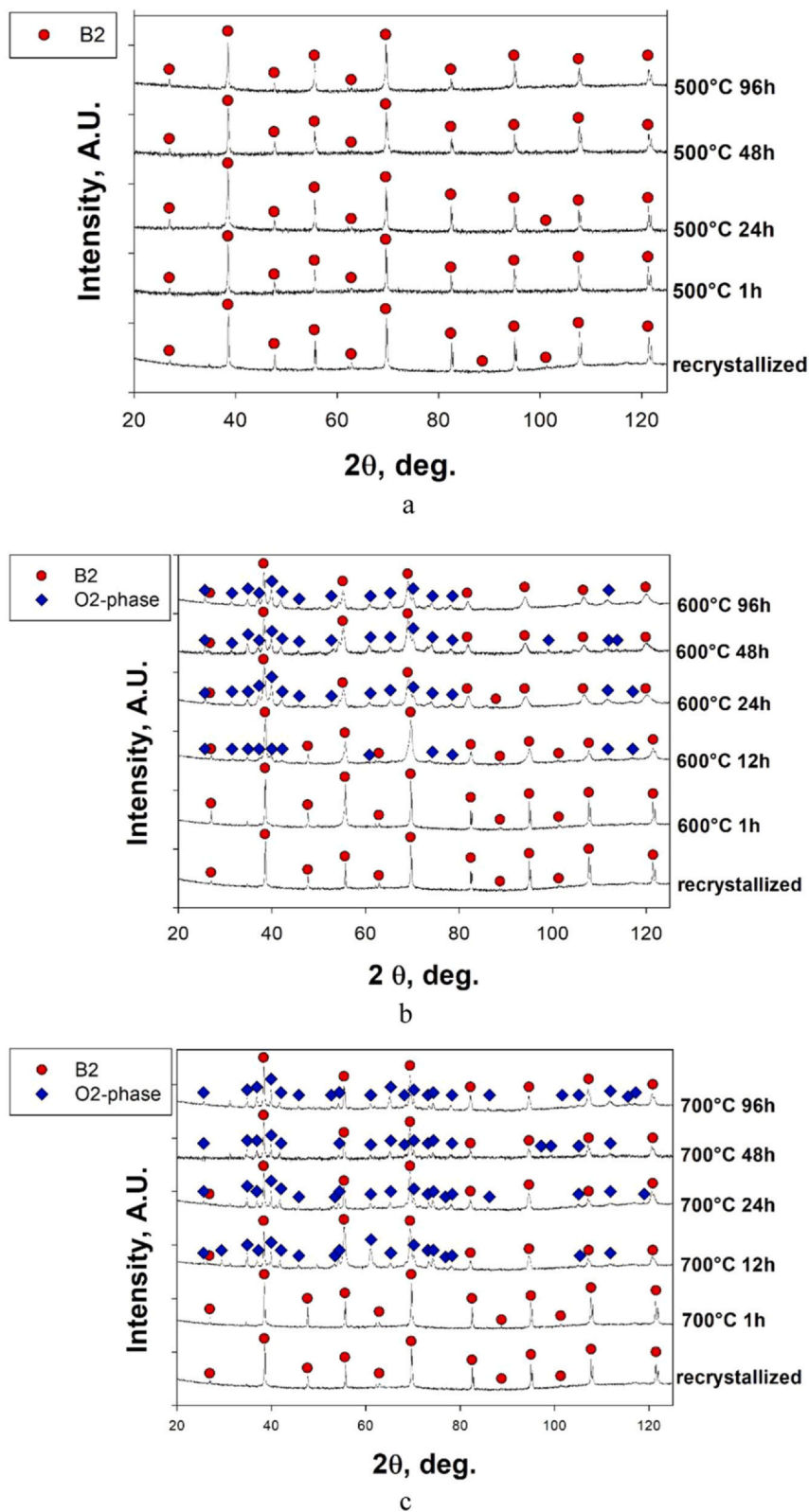


Fig. 4. XRD patterns of the $\text{Ti}_{40}\text{Nb}_{30}\text{Hf}_{15}\text{Al}_{15}$ alloy in the recrystallized condition and after aging at 500 (a), 600 (b), 700 °C (c).

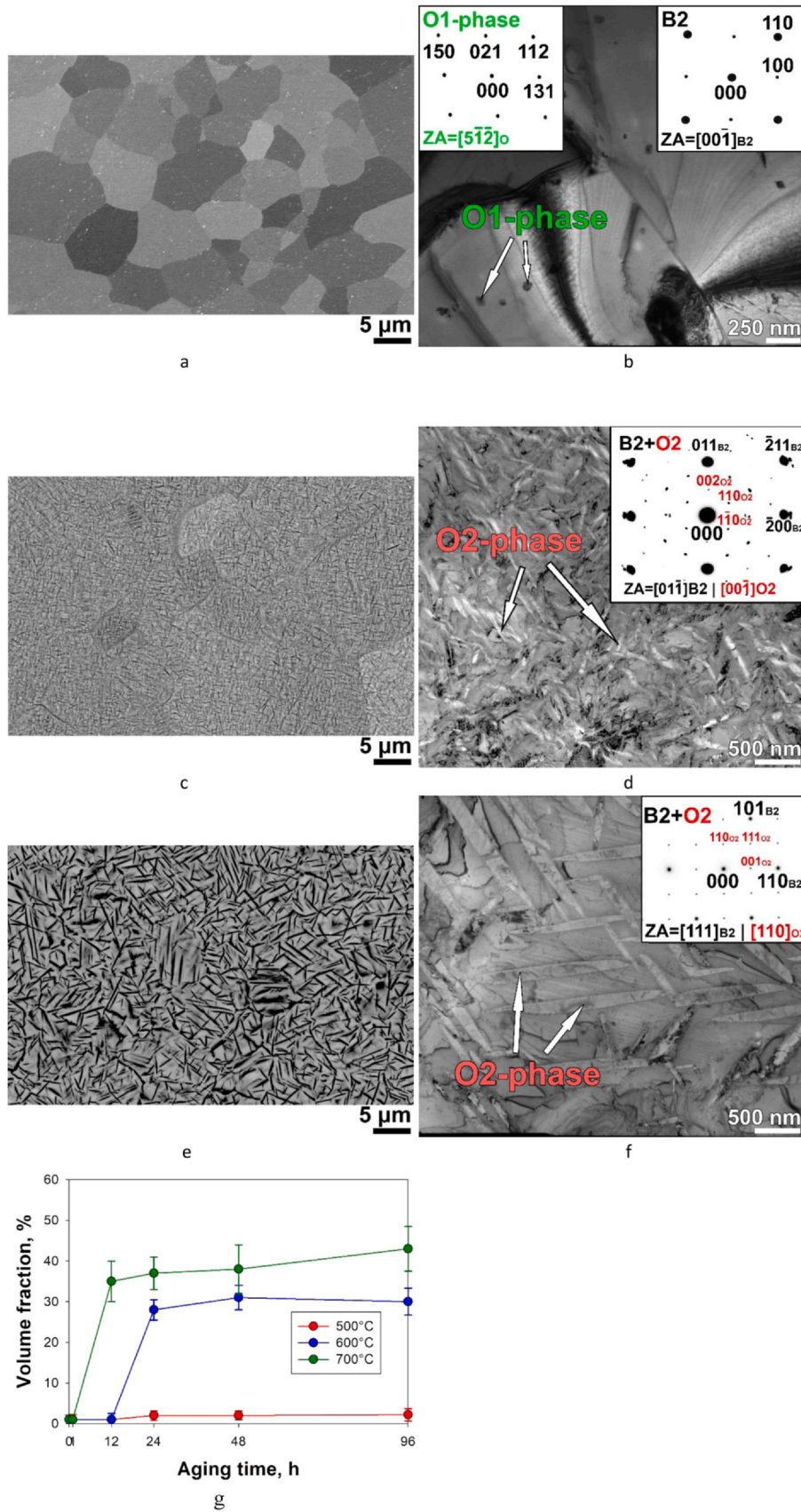


Fig. 5. Microstructure of the $Ti_{40}Nb_{30}Hf_{15}Al_{15}$ alloy after aging at 500 (a, b), 600 (c, d), 700 °C (e, f) for 24 h: a, c, e – SEM-BSE images; b, d, f – TEM bright-field images with SAEDs of the B2, O1-, and O2-phases; dependence of the volume fraction of secondary phase(s) particles on aging conditions (g).

Table 3
Measured chemical composition of the structural constituents in the Ti₄₀Nb₃₀Hf₁₅Al₁₅ alloy after aging at 500, 600, 700 °C.

Condition	Phase	Fraction, %	Chemical composition, at%				Average size, μm	
			Ti	Nb	Hf	Al	Transversal	Longitudinal
Aged at 500 °C, 24 h	B2	98.5	43.2	29.0	14.3	13.5	5.1 ± 2.0	
	O1-phase	1.5	22.0	14.3	63.7	0	0.05 ± 0.02	0.07 ± 0.03
	Nominal	–	42.8	28.8	15.2	13.2	–	–
Aged at 600 °C, 24 h	B2	72	37.9	32.7	17.8	11.6	6.5 ± 3.5	
	O2-phase	28	43.3	21.0	10.1	25.6	0.08 ± 0.03	0.7 ± 0.3
	Nominal	–	42.8	28.8	15.2	13.2	–	–
Aged at 700 °C, 24 h	B2	63	40.0	27.8	21.4	10.8	7.7 ± 2.7	
	O2-phase	37	43.2	18.5	10.1	28.2	0.4 ± 0.1	3.1 ± 1.3
	Nominal	–	42.8	28.8	15.2	13.2	–	–

composition and a wider precipitation window than the O2-phase. The O1-phase is a disordered Hf-rich and Al-free phase found in the recrystallized state and after aging at 500 °C, while the O2-phase is an ordered (Ti, Al)-rich phase precipitated at 600 and 700 °C. It can be speculated that a three-phase B2 + O1 + O2 structure exists in the 600–700 °C temperature interval. However, the massive O2-phase formation hinders the unambiguous identification of the O1-phase in this region. The upper solvus temperature and precipitation kinetics of the O1-phase also remains questionable. A previous study [42] did not reveal the O1-phase after annealing at 1200 °C for 24 h, thus suggesting 900–1200 °C as a possible temperature range for the O1 phase solvus.

Particular attention should also be paid to the precipitation range of the O2-phase in the Ti₄₀Nb₃₀Hf₁₅Al₁₅ alloy. As mentioned above, no O2-phase was found at T ≥ 900 °C, while the massive O2-phase appeared at 600 and 700 °C, respectively. Such a narrow stability interval of the O2-phase is typical for the Ti₂AlNb alloys with a high Nb and a low Al content rather than for stoichiometric or near-stoichiometric Ti₂AlNb compositions [51–53]. Specifically, similar behavior was observed for a Ti₅₀Nb₃₈Al₁₂ alloy by Boehlert et al. [52]. It was reported that the Ti₅₀Nb₃₈Al₁₂ alloy had a single-phase bcc structure after annealing at 900–1200 °C, which transformed into the bcc+O2 mixture during subsequent aging at 650–800 °C. Moreover, the precipitation kinetics of the Ti₄₀Nb₃₀Hf₁₅Al₁₅ and Ti₅₀Nb₃₈Al₁₂ alloys is also comparable. In both alloys, the O2-phase volume fraction is closely related to aging duration. Being relatively small after short-term annealing, it increases to a certain level and remains almost constant after 12–24 h at 600–700 °C and ~50 h at 650 °C in the Ti₄₀Nb₃₀Hf₁₅Al₁₅ and Ti₅₀Nb₃₈Al₁₂ alloys, respectively. Bearing in mind the stability of the bcc+O2 structure of the Ti₅₀Nb₃₈Al₁₂ alloy after a relatively long-term (434 h) aging at 650 °C, we can expect an analogous behavior of the Ti₄₀Nb₃₀Hf₁₅Al₁₅ alloy at 600–700 °C.

Meanwhile, the particles precipitated after annealing at 600–700 °C in the alloys with Hf/Zr have distinctively different morphology. The O2-particles have a characteristic lens shape and are relatively thin, while the Zr₅Al₃-type particles are equiaxed and quite coarse. The lens-shaped morphology of the O2-phase is typical for the Ti₂AlNb-based alloys and can be attributed to the specific OR between the bcc/B2 matrix and the particles, namely [011̄]_{B2}||[001̄]_{O2}, (2̄11)_{B2}||[(110)_{O2} and [111]_{B2}||[(110)_{O2}, (110)_{B2}||[(001)_{O2} [52,53]. The same ORs were found in the Ti₄₀Nb₃₀Hf₁₅Al₁₅ alloy (Fig. 5d and f). In turn, Zr₅Al₃-type particles in bcc/B2-based RHEAs often have a similar morphology to those observed in the Ti₄₀Nb₃₀Zr₂₀Al₁₀ alloy [19,47,54].

The effect of heat treatment on the mechanical properties of the program alloys was also diverse. Although annealing at 500 °C barely affected the hardness of both alloys, annealing at 600 and 700 °C

resulted in hardening of the Ti₄₀Nb₃₀Hf₁₅Al₁₅ alloy (significant – at 600 °C), while the Ti₄₀Nb₃₀Zr₂₀Al₁₀ softened. The changes in hardness can be most probably attributed to the secondary phases' precipitation. The effect of equiaxed O1/Zr₅Al₃ precipitates on the strength via the Orowan mechanism can be considered using the following equation [55]:

$$\Delta\sigma_{or} = \left(0.538Gb\frac{1}{d}\right)\ln(d/2b) \quad (1)$$

where b is the Burgers vector, G is the shear modulus, and f and d are the particle fraction and size, respectively.

The contribution of the lens-shaped O2-particle to the overall strength can be estimated following a modified Ashby-Orowan equation [56]:

$$\Delta\sigma_{or} = \frac{0.538Gb}{2.36\pi} \ln\left(\frac{0.57DS^{\frac{1}{3}}}{b}\right) \frac{1}{\left(0.92V^{-\frac{1}{3}} - 1.14\right)DS^{\frac{1}{3}}} \quad (2)$$

where G is the shear modulus ($G = 37.4$ GPa) calculated using the rule of mixture; b is the Burgers vector estimated using the experimental bcc lattice parameter; S is the aspect ratio of O2-phase particles (at 600 °C $S = 10.5$ and at 700 °C $S = 16.2$); D is the transversal size of the O2-phase particles; V is the volume fraction of the O2-phase particles.

To estimate the effect of the precipitates on the mechanical properties, the strengthening effect in the recrystallized and aged for 24 h conditions was calculated using Eqs. (1) and (2) and converted to HV. Then, the difference in the predicted hardening between the aged and recrystallized condition (ΔHV_{or}) was calculated and compared with the experimental data (ΔHV_{exp}). The obtained results are presented in Fig. 9.

Comparing the strengthening predicted using the Orowan mechanism and experimental values has revealed good agreement (Fig. 9). This is the indication that, for example, a sharp increase in the hardness of the Ti₄₀Nb₃₀Hf₁₅Al₁₅ after annealing at 600 °C can be attributed to precipitation of the fine O2-phase particles after 24 h of annealing and their stability.

However, the reasons for the softening of the Ti₄₀Nb₃₀Zr₂₀Al₁₀ alloy cannot be explained using the Orowan equation. Probably, they can be ascribed to the variations in the chemical composition of the B2 matrix phase (Tables 2 and 4) and associated solid solution strengthening (SSS). The SSS in (R)HEAs has been long discussed as a very potent source of strengthening. However, due to the chemical complexity, analytical models for SSS in HEAs were not developed until recently [9,57–60]. Here, we have used the Coury-Kaufman-Clark model [9], which has recently been proven accurate for the

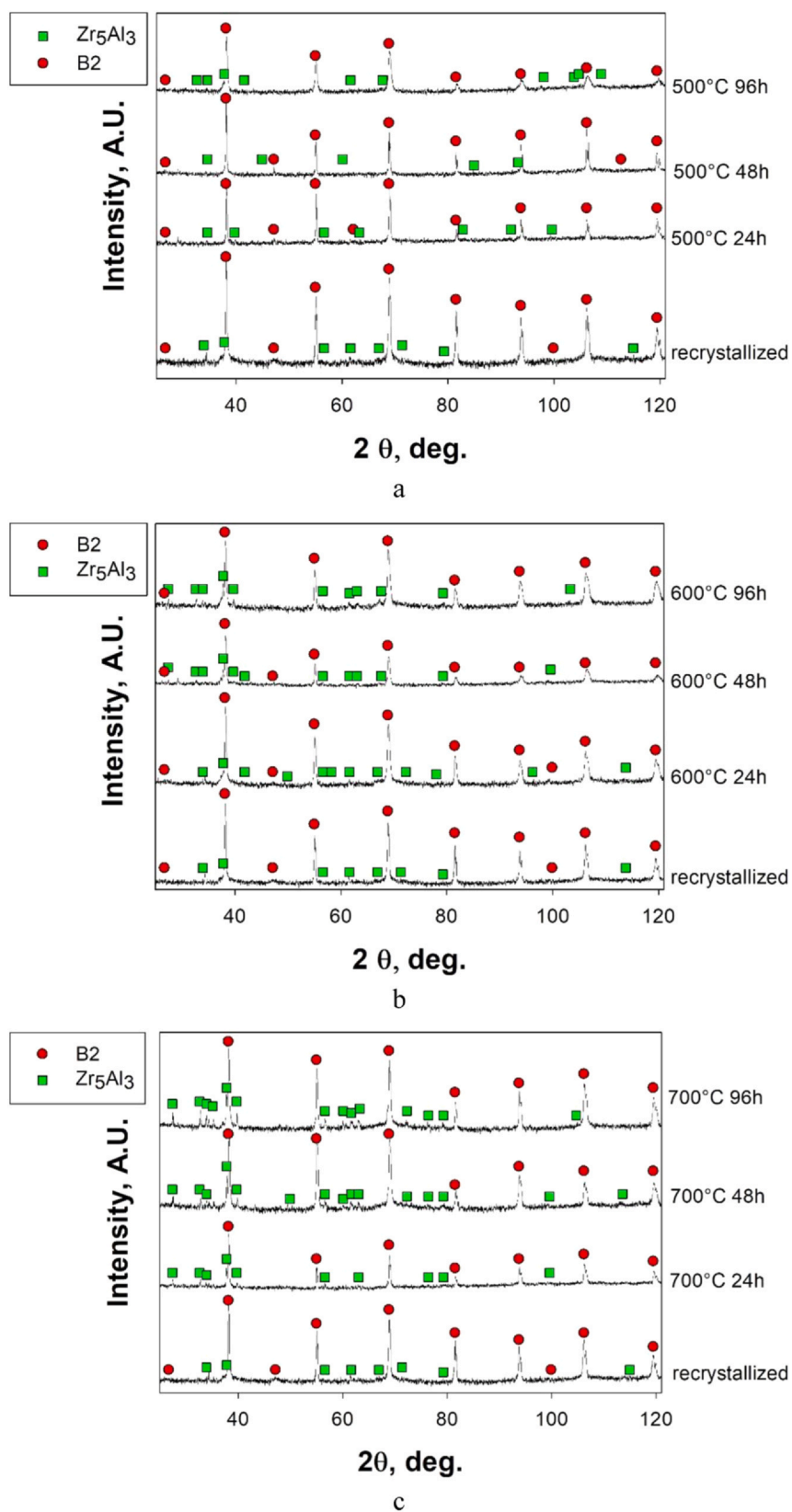


Fig. 6. XRD patterns of the $\text{Ti}_{40}\text{Nb}_{30}\text{Zr}_{20}\text{Al}_{10}$ alloy in the recrystallized condition and after aging at 500 (a), 600 (b), 700 °C (c).

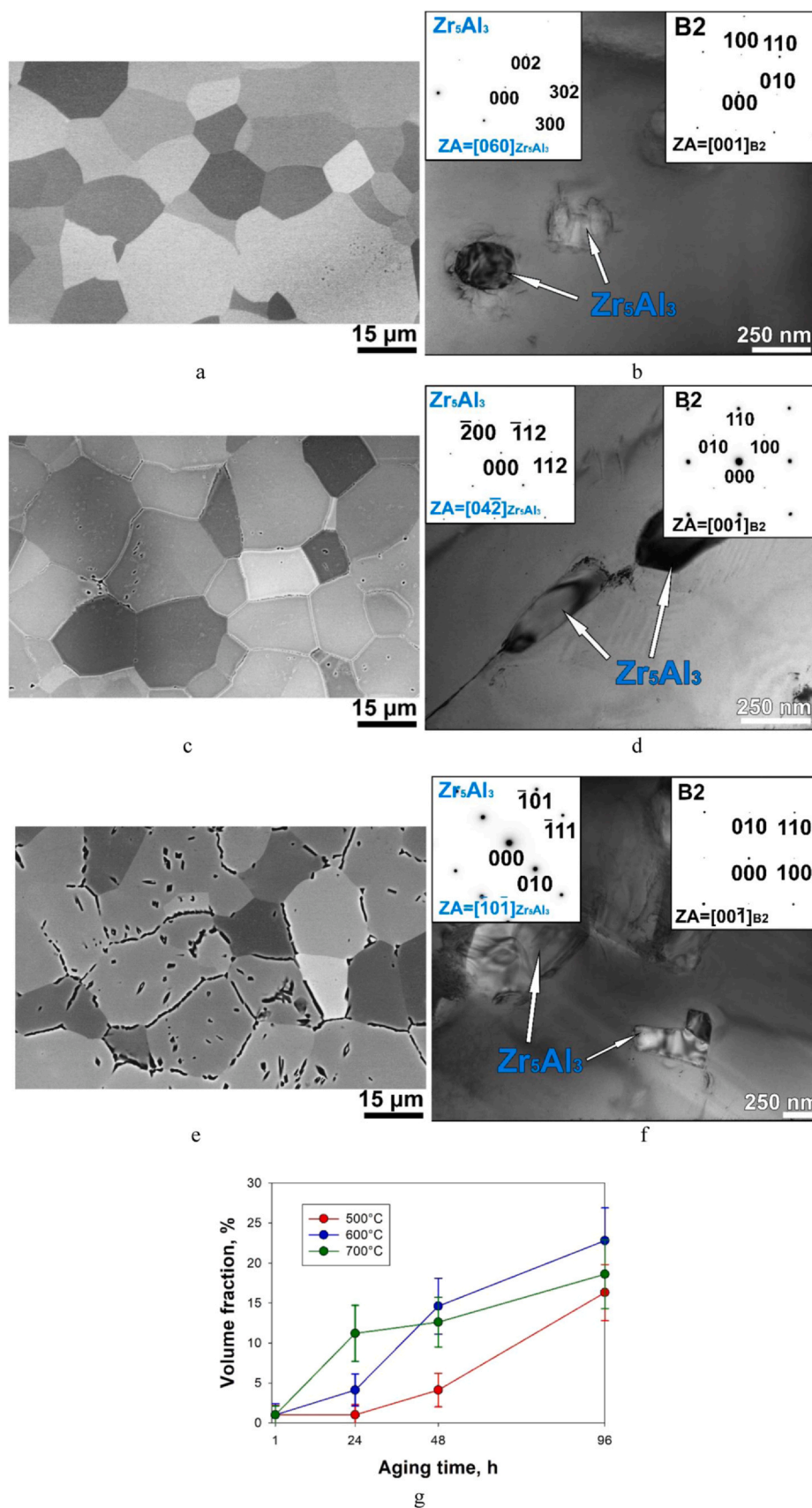
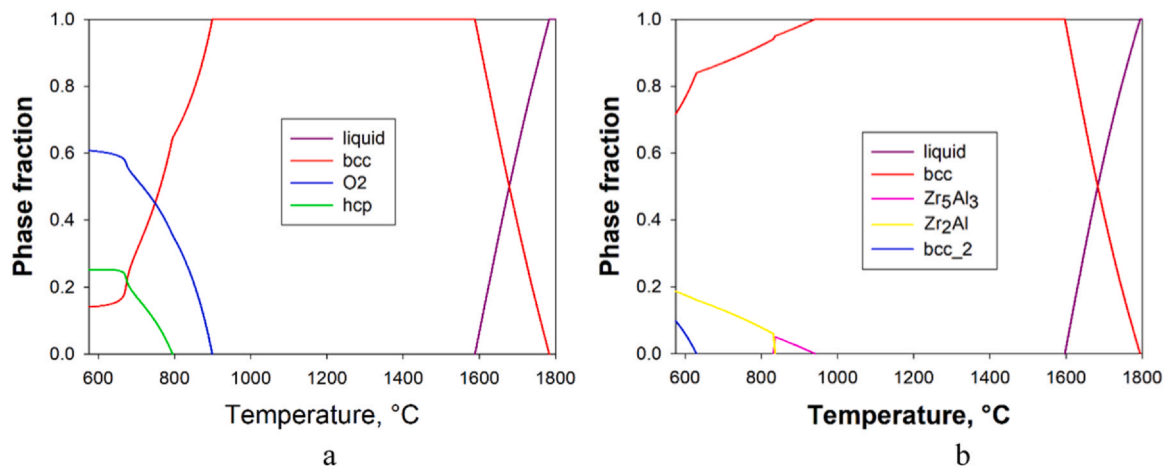


Fig. 7. Microstructure of the $Ti_{40}Nb_{30}Zr_{20}Al_{10}$ alloy after aging at 500 (a, b), 600 (c, d), 700 °C (e, f) for 24 h: a, c, e – SEM-BSE images; b, d, f – TEM bright-field images with SAEDs of the B2 and Zr_5Al_3 -type phases; dependence of the volume fraction of the Zr_5Al_3 -type particles on aging conditions (e).

Table 4Measured chemical composition of the structural constituents in the $\text{Ti}_{40}\text{Nb}_{30}\text{Zr}_{20}\text{Al}_{10}$ alloy after aging at 500, 600, 700 °C.

Condition	Phase	Fraction, %	Chemical composition, at%				Average size, μm	
			Ti	Nb	Zr	Al	Transversal	Longitudinal
Aging at 500 °C, 24 h	B2	98.2	42.2	28.9	19.5	9.4	14.7 ± 7.7	
	Zr_5Al_3	1.8	18.8	14.3	38.4	28.5	0.3 ± 0.1	0.3 ± 0.1
	Nominal	–	41.2	28.6	20.1	10.1	–	
Aging at 600 °C, 24 h	B2	94.7	42.5	29.7	18.5	9.3	13.6 ± 7.1	
	Zr_5Al_3	5.3	12.4	10.6	44.4	32.6	0.3 ± 0.1	0.6 ± 0.2
	Nominal	–	41.2	28.6	20.1	10.1	–	
Aging at 700 °C, 24 h	B2	89.5	44.0	30.7	17.8	7.5	13.4 ± 7.0	
	Zr_5Al_3	10.5	13.4	9.4	39.9	37.3	0.6 ± 0.2	1.7 ± 0.7
	Nominal	–	41.2	28.6	20.1	10.1	–	

**Fig. 8.** Equilibrium phase diagrams of the $\text{Ti}_{40}\text{Nb}_{30}\text{Hf}_{15}\text{Al}_{15}$ (a) and $\text{Ti}_{40}\text{Nb}_{30}\text{Zr}_{20}\text{Al}_{10}$ (b) alloys.**Table 5**Predicted phase fractions and chemical compositions of the $\text{Ti}_{40}\text{Nb}_{30}\text{Hf}_{15}\text{Al}_{15}$ and $\text{Ti}_{40}\text{Nb}_{30}\text{Zr}_{20}\text{Al}_{10}$ alloys in the recrystallized condition and after annealing at 500, 600, 700 °C.

Alloy	$T, ^\circ\text{C}$	Phase	Fraction, %	Chemical composition, at%				
				Ti	Nb	Hf	Zr	Al
$\text{Ti}_{40}\text{Nb}_{30}\text{Hf}_{15}\text{Al}_{15}$	900	bcc	100	40	30	15	–	15
	500	bcc	14.0	6.5	91.9	1.3	–	0.3
		hcp	28.2	38.9	1.1	59.7	–	0.3
		O-phase	57.8	48.1	27.6	0	–	24.3
	600	bcc	14.3	10.5	85.3	3.0	–	1.2
		hcp	28.4	39.4	1.9	57.8	–	0.9
		O-phase	57.3	47.2	28.7	0	–	24.1
	700	bcc	31.2	33.0	45.6	15.0	–	6.4
		hcp	19.4	34.1	2.8	60.7	–	2.4
O-phase		49.4	46.1	29.7	0	–	24.2	
$\text{Ti}_{40}\text{Nb}_{30}\text{Zr}_{20}\text{Al}_{10}$	900	bcc	98.0	40.6	30.6	–	19.4	9.4
	500	Zr_5Al_3	2.0	11.6	0	–	50.9	37.5
		bcc	31.2	10.0	88.6	–	1.2	0.2
		Zr_2Al	17.8	9.6	0	–	57.1	33.3
	600	hcp	51.0	68.9	4.8	–	18.4	7.9
		bcc	76.6	48.4	32.9	–	13.3	5.4
		bcc_2	5.9	15.5	81.2	–	2.6	0.7
	700	Zr_2Al	17.5	11.3	0	–	55.3	33.4
		bcc	87.0	44.1	34.5	–	14.9	6.5
		Zr_2Al	13.0	12.4	0	–	54.3	33.3

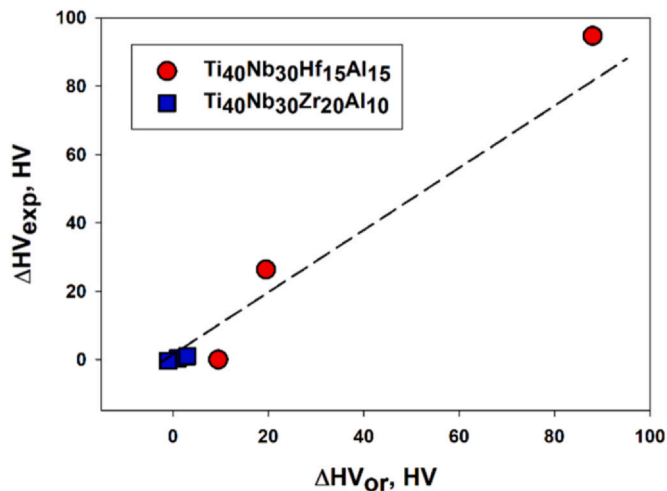


Fig. 9. The comparison between the experimental (ΔHV_{exp}) and predicted (via the Orowan mechanism, ΔHV_{or}) changes in the alloys' hardness after aging treatment for 24 h at different temperatures.

Hf-Nb-Ta-Ti-Zr RHEAs [61], to calculate SSS for the B2 matrix phase of the $Ti_{40}Nb_{30}Zr_{20}Al_{10}$ alloy in the recrystallized condition (the corresponding chemical composition is given in Table 2) and after annealing at 700 for 24 h (Table 4). After converting to HV, the difference between the two values is about 6 HV, which correlates well with the experimental difference of 7 HV. Thus, it is reasonable to suggest that the observed softening is indeed due to changes in the chemical composition of the matrix phase and the weakening of the SSS. Note, however, that these are very rude estimates that can be inaccurate due to B2 ordered structure of the matrix phase, while the existing SSS models were developed for random solid solution.

5. Conclusions

In the present work, structure and mechanical properties of the $Ti_{40}Nb_{30}Hf_{15}Al_{15}$ and $Ti_{40}Nb_{30}Zr_{20}Al_{10}$ refractory high entropy alloys after cold rolling to 80% reduction, recrystallization annealing at 900 °C for 15 min, and further aging treatment at $T = 500, 600$ and 700 °C for 1–96 h were studied. The following conclusions were drawn:

- 1) In the as-cast condition, both alloys had a coarse-grained (445–470 μm) single B2 phase structure. After cold rolling and annealing at 900 °C for 15 min, the B2 grain size was considerably refined to 4.3 ± 2.2 and $13.2 \pm 5.0 \mu m$ in the $Ti_{40}Nb_{30}Hf_{15}Al_{15}$ and $Ti_{40}Nb_{30}Zr_{20}Al_{10}$ alloys, respectively. In addition, a small fraction (< 1%) of the Hf-rich disordered orthorhombic (O1) and Zr_5Al_3 -type phases appeared, respectively, in the alloys with Hf and Zr.
- 2) Annealing at 500 °C has barely affected the recrystallized structure of the $Ti_{40}Nb_{30}Hf_{15}Al_{15}$ alloy; meanwhile, the annealing at 600 °C for 24 h and more and 700 °C for 12 h and more has resulted in massive precipitation of the ordered orthorhombic (O2) phase. The O2 particles were enriched with Al and Ti and had characteristic lens-shaped morphology. The thickness of the O2 particles increased pronouncedly when the annealing temperature increased from 600 to 700 °C. The following orientation relationships between the B2 matrix and the O2 precipitates were found: $[01\bar{1}]_{B2} \parallel [00\bar{1}]_{O2}$, $(\bar{2}11)_{B2} \parallel (110)_{O2}$ and $[111]_{B2} \parallel [110]_{O2}$, $(110)_{B2} \parallel (001)_{O2}$.
- 3) Annealing of the $Ti_{40}Nb_{30}Zr_{20}Al_{10}$ alloy at 500–700 °C resulted in the precipitation of additional Zr_5Al_3 -type phase particles. The volume fraction of the Zr_5Al_3 -type phase increased continuously with annealing time. The size of the particles increased with increasing annealing temperature.

- 4) The phases found in the $Ti_{40}Nb_{30}Hf_{15}Al_{15}$ and $Ti_{40}Nb_{30}Zr_{20}Al_{10}$ alloys are in reasonable agreement with the CALPHAD predictions.
- 5) The microhardness of the $Ti_{40}Nb_{30}Hf_{15}Al_{15}$ increased considerably after annealing at 600 °C for 24 h and more due to precipitation hardening by the O2-phase particles. Annealing at 500 and 700 °C had a weak effect on the hardness of the alloy. Meanwhile, the microhardness of the $Ti_{40}Nb_{30}Zr_{20}Al_{10}$ alloy decreased after annealing at 600 and 700 °C. The decrease in hardness is likely associated with the weakened solid solution hardening in the B2 matrix.

CRedit authorship contribution statement

E. Panina: Investigation, Methodology, Validation, Writing – original draft. **N. Yurchenko:** Investigation, Discussion, Writing – review & editing. **S. Zhrebtsov:** Conceptualization, Writing – review & editing, Supervision. **N. Stepanov:** Investigation, Writing – review & editing, Discussion.

Declaration of Competing Interest

The authors declare that they have no known competing financial interests or personal relationships that could have appeared to influence the work reported in this paper.

Acknowledgments

The authors gratefully acknowledge the financial support from the Russian Science Foundation Grant № 19-79-30066. The authors would like to express their gratitude to Dr. Dmitry Shaysultanov and Mr. Denis Klimenko for their help with experiments and calculations. The authors are grateful to the personnel of the Joint Research Center, "Technology and Materials", Belgorod State National Research University, for their assistance with the instrumental analysis.

References

- [1] J.H. Perepezko, The hotter the engine, the better, *Science* (80-.) 326 (2009) 1068–1069, <https://doi.org/10.1126/science.1179327>
- [2] O.N. Senkov, G.B. Wilks, D.B. Miracle, C.P. Chuang, P.K. Liaw, Refractory high-entropy alloys, *Intermetallics* 18 (2010) 1758–1765, <https://doi.org/10.1016/j.intermet.2010.05.014>
- [3] O.N. Senkov, G.B. Wilks, J.M. Scott, D.B. Miracle, Mechanical properties of Nb25Mo25Ta25W25 and V20Nb20Mo20Ta20W20 refractory high entropy alloys, *Intermetallics* 19 (2011) 698–706, <https://doi.org/10.1016/j.intermet.2011.01.004>
- [4] N.D. Stepanov, D.G. Shaysultanov, G.A. Salishchev, M.A. Tikhonovsky, Structure and mechanical properties of a light-weight AlNbTiV high entropy alloy, *Mater. Lett.* 142 (2015) 153–155, <https://doi.org/10.1016/j.matlet.2014.11.162>
- [5] C.M. Lin, C.C. Juan, C.H. Chang, C.W. Tsai, J.W. Yeh, Effect of Al addition on mechanical properties and microstructure of refractory AlxHfNbTaTiZr alloys, *J. Alloy. Compd.* 624 (2015) 100–107, <https://doi.org/10.1016/j.jallcom.2014.11.064>
- [6] B. Gorr, M. Azim, H.J. Christ, T. Mueller, D. Schliephake, M. Heilmaier, Phase equilibria, microstructure, and high temperature oxidation resistance of novel refractory high-entropy alloys, *J. Alloy. Compd.* 624 (2015) 270–278, <https://doi.org/10.1016/j.jallcom.2014.11.012>
- [7] D.B. Miracle, O.N. Senkov, A critical review of high entropy alloys and related concepts, *Acta Mater.* 122 (2017) 448–511, <https://doi.org/10.1016/j.actamat.2016.08.081>
- [8] O.N. Senkov, D.B. Miracle, K.J. Chaput, J.P. Couzinie, Development and exploration of refractory high entropy alloys – a review, *J. Mater. Res.* 33 (2018) 3092–3128, <https://doi.org/10.1557/jmr.2018.153>
- [9] F.G. Coury, M. Kaufman, A.J. Clarke, Solid-solution strengthening in refractory high entropy alloys, *Acta Mater.* 175 (2019) 66–81, <https://doi.org/10.1016/j.actamat.2019.06.006>
- [10] H. Chen, A. Kauffmann, S. Seils, T. Boll, C.H. Liebscher, I. Harding, K.S. Kumar, D.V. Szabó, S. Schlabach, S. Kauffmann-Weiss, F. Müller, B. Gorr, H.J. Christ, M. Heilmaier, Crystallographic ordering in a series of Al-containing refractory high entropy alloys Ta–Nb–Mo–Cr–Ti–Al, *Acta Mater.* 176 (2019) 123–133, <https://doi.org/10.1016/j.actamat.2019.07.001>
- [11] N. Shkodich, A. Sedegov, K. Kuskov, S. Busurin, Y. Scheck, S. Vadchenko, D. Moskovskikh, Refractory high-entropy hftainbcr-based alloys by combined use of ball milling and spark plasma sintering: effect of milling intensity, *Metals* 10 (2020) 1–15, <https://doi.org/10.3390/met10091268>

- [12] X.W. Liu, Z.C. Bai, X.F. Ding, J.Q. Yao, L. Wang, Y.Q. Su, Z.T. Fan, J.J. Guo, A novel light-weight refractory high-entropy alloy with high specific strength and intrinsic deformability, *Mater. Lett.* 287 (2021) 129255, <https://doi.org/10.1016/j.matlet.2020.129255>
- [13] Q. Wang, J. Han, Y. Liu, Z. Zhang, C. Dong, P.K. Liaw, Coherent precipitation and stability of cuboidal nanoparticles in body-centered-cubic Al_{0.4}Nb_{0.5}Ta_{0.5}TiZr_{0.8} refractory high entropy alloy, *Scr. Mater.* 190 (2021) 40–45, <https://doi.org/10.1016/j.scriptamat.2020.08.029>
- [14] S. Chen, K.K. Tseng, Y. Tong, W. Li, C.W. Tsai, J.W. Yeh, P.K. Liaw, Grain growth and Hall-Petch relationship in a refractory HfNbTaZrTi high-entropy alloy, *J. Alloy. Compd.* 795 (2019) 19–26, <https://doi.org/10.1016/j.jallcom.2019.04.291>
- [15] K.K. Tseng, C.C. Juan, S. Tso, H.C. Chen, C.W. Tsai, J.W. Yeh, Effects of Mo, Nb, Ta, Ti, and Zr on mechanical properties of equiatomic Hf-Mo-Nb-Ta-Ti-Zr alloys, *Entropy* 21 (2019) 15, <https://doi.org/10.3390/e21010015>
- [16] H. Yao, Y. Liu, X. Sun, Y. Lu, T. Wang, T. Li, Microstructure and mechanical properties of Ti₃V₂NbAl Ni low-density refractory multielement alloys, *Intermetallics* 133 (2021) 107187, <https://doi.org/10.1016/j.intermet.2021.107187>
- [17] Y. Lu, H. Huang, X. Gao, C. Ren, J. Gao, H. Zhang, S. Zheng, Q. Jin, Y. Zhao, C. Lu, T. Wang, T. Li, A promising new class of irradiation tolerant materials: Ti₂ZrHfV_{0.5}Mo_{0.2} high-entropy alloy, *J. Mater. Sci. Technol.* 35 (2019) 369–373, <https://doi.org/10.1016/j.jmst.2018.09.034>
- [18] H. Yao, J. Miao, Y. Liu, E. Guo, H. Huang, Y. Lu, T. Wang, T. Li, Effect of Ti and Nb contents on microstructure and mechanical properties of HfZrV_{0.5}TaMoW_{0.5}Nb_{0.5} refractory high-entropy alloys, *Adv. Eng. Mater.* (2021) 2100225, <https://doi.org/10.1002/adem.202100225>
- [19] N.Y. Yurchenko, N.D. Stepanov, A.O. Gridneva, M.V. Mishunin, G.A. Salishchev, S.V. Zherebtsov, Effect of Cr and Zr on phase stability of refractory Al-Cr-Nb-Ti-V-Zr high-entropy alloys, *J. Alloy. Compd.* 757 (2018) 403–414, <https://doi.org/10.1016/j.jallcom.2018.05.099>
- [20] Q.Q. Wei, X.D. Xu, G.M. Li, G.Q. Luo, J. Zhang, Q. Shen, C.L. Wu, A carbide-reinforced Re_{0.5}MoNbW(TaC)_{0.8} eutectic high-entropy composite with outstanding compressive properties, *Scr. Mater.* 200 (2021) 113909, <https://doi.org/10.1016/j.scriptamat.2021.113909>
- [21] M. Wang, Z.L. Ma, Z.Q. Xu, X.W. Cheng, Designing VxNbMoTa refractory high-entropy alloys with improved properties for high-temperature applications, *Scr. Mater.* 191 (2021) 131–136, <https://doi.org/10.1016/j.scriptamat.2020.09.027>
- [22] F. Wang, G.H. Balbus, S. Xu, Y. Su, J. Shin, P.F. Rottmann, K.E. Knipling, J.C. Stinville, L.H. Mills, O.N. Senkov, I.J. Beyerlein, T.M. Pollock, D.S. Gianola, Multiplicity of dislocation pathways in a refractory multiprincipal element alloy, *Science* (80-.) 370 (2020) 95–101, <https://doi.org/10.1126/science.aba3722>
- [23] S.Y. Chen, L. Wang, W.D. Li, Y. Tong, K.K. Tseng, C.W. Tsai, J.W. Yeh, Y. Ren, W. Guo, J.D. Poplawsky, P.K. Liaw, Peierls barrier characteristic and anomalous strain hardening provoked by dynamic-strain-aging strengthening in a body-centered-cubic high-entropy alloy, *Mater. Res. Lett.* 7 (2019) 475–481, <https://doi.org/10.1080/21663831.2019.1658233>
- [24] E. Panina, N. Yurchenko, S. Zherebtsov, G. Salishchev, N. Stepanov, Precipitation-hardened refractoryTi-Nb-Hf-Al-Ta high-entropy alloys, *IOP Conf. Ser.: Mater. Sci. Eng.* 1014 (2021) 012041, <https://doi.org/10.1088/1757-899X/1014/1/012041>
- [25] N.D. Stepanov, N.Y. Yurchenko, D.V. Skibin, M.A. Tikhonovsky, G.A. Salishchev, Structure and mechanical properties of the AlCr_xNbTiV ($x = 0, 0.5, 1, 1.5$) high entropy alloys, *J. Alloy. Compd.* 652 (2015) 266–280, <https://doi.org/10.1016/j.jallcom.2015.08.224>
- [26] O.N. Senkov, S.V. Senkova, D.B. Miracle, C. Woodward, Mechanical properties of low-density, refractory multi-principal element alloys of the Cr-Nb-Ti-V-Zr system, *Mater. Sci. Eng. A.* 565 (2013) 51–62, <https://doi.org/10.1016/j.msea.2012.12.018>
- [27] N. Yurchenko, E. Panina, S. Zherebtsov, N. Stepanov, Design and characterization of eutectic refractory high entropy alloys, *Materialia* 16 (2021) 101057, <https://doi.org/10.1016/j.mtla.2021.101057>
- [28] Roger C. Reed, *The Superalloys: Fundamentals and Applications*, Cambridge University Press, 2006.
- [29] A.J. Knowles, L. Reynolds, V.A. Vorontsov, D. Dye, A nickel based superalloy reinforced by both Ni₃Al and Ni₃V ordered-fcc precipitates, *Scr. Mater.* 162 (2019) 472–476, <https://doi.org/10.1016/j.scriptamat.2018.12.013>
- [30] D.B. Miracle, M.H. Tsai, O.N. Senkov, V. Soni, R. Banerjee, Refractory high entropy superalloys (RSAs), *Scr. Mater.* 187 (2020) 445–452, <https://doi.org/10.1016/j.scriptamat.2020.06.048>
- [31] Y.T. Chen, Y.J. Chang, H. Murakami, S. Gorsse, A.C. Yeh, Designing high entropy superalloys for elevated temperature application, *Scr. Mater.* 187 (2020) 177–182, <https://doi.org/10.1016/j.scriptamat.2020.06.002>
- [32] T.E. Whitfield, E.J. Pickering, K.A. Christofidou, C.N. Jones, H.J. Stone, N.G. Jones, Elucidating the microstructural development of refractory metal high entropy superalloys via the Ti-Ta-Zr constituent system, *J. Alloy. Compd.* 818 (2020) 152935, <https://doi.org/10.1016/j.jallcom.2019.152935>
- [33] S. Chen, Q. Li, J. Zhong, F. Xing, L. Zhang, On diffusion behaviors in face centered cubic phase of Al-Co-Cr-Fe-Ni-Ti high-entropy superalloys, *J. Alloy. Compd.* 791 (2019) 255–264, <https://doi.org/10.1016/j.jallcom.2019.03.286>
- [34] J.J. Yang, C.M. Kuo, P.T. Lin, H.C. Liu, C.Y. Huang, H.W. Yen, C.W. Tsai, Improvement in oxidation behavior of Al_{0.2}Co_{1.5}CrFeNi_{1.5}Ti_{0.3} high-entropy superalloys by minor Nb addition, *J. Alloy. Compd.* 825 (2020) 153983, <https://doi.org/10.1016/j.jallcom.2020.153983>
- [35] L. Zhang, Y. Zhou, X. Jin, X. Du, B. Li, The microstructure and high-temperature properties of novel nano precipitation-hardened face centered cubic high-entropy superalloys, *Scr. Mater.* 146 (2018) 226–230, <https://doi.org/10.1016/j.scriptamat.2017.12.001>
- [36] T.E. Whitfield, E.J. Pickering, C.E. Talbot, C.N. Jones, H.J. Stone, N.G. Jones, Observation of a refractory metal matrix containing Zr-Ti-rich precipitates in a Mo_{0.5}NbTa_{0.5}TiZr high entropy alloy, *Scr. Mater.* 180 (2020) 71–76, <https://doi.org/10.1016/j.scriptamat.2020.01.028>
- [37] O.N. Senkov, S.V. Senkova, C. Woodward, Effect of aluminum on the microstructure and properties of two refractory high-entropy alloys, *Acta Mater.* 68 (2014) 214–228, <https://doi.org/10.1016/j.actamat.2014.01.029>
- [38] D. Schliephake, A.E. Medvedev, M.K. Imran, S. Obert, D. Fabijanic, M. Heilmairer, A. Molotnikov, X. Wu, Precipitation behaviour and mechanical properties of a novel Al_{0.5}MoTaTi complex concentrated alloy, *Scr. Mater.* 173 (2019) 16–20, <https://doi.org/10.1016/j.scriptamat.2019.07.033>
- [39] V. Soni, O.N. Senkov, B. Gwalani, D.B. Miracle, R. Banerjee, Microstructural design for improving ductility of an initially brittle refractory high entropy alloy, *Sci. Rep.* 8 (2018) 1–10, <https://doi.org/10.1038/s41598-018-27144-3>
- [40] T.E. Whitfield, E.J. Pickering, L.R. Owen, O.N. Senkov, D.B. Miracle, H.J. Stone, N.G. Jones, An assessment of the thermal stability of refractory high entropy superalloys, *J. Alloy. Compd.* 857 (2021) 157583, <https://doi.org/10.1016/j.jallcom.2020.157583>
- [41] T.E. Whitfield, E.J. Pickering, L.R. Owen, C.N. Jones, H.J. Stone, N.G. Jones, The effect of Al on the formation and stability of a BCC - B2 microstructure in a refractory metal high entropy superalloy system, *Materialia* 13 (2020) 100858, <https://doi.org/10.1016/j.mtla.2020.100858>
- [42] N. Yurchenko, E. Panina, M. Tikhonovsky, G. Salishchev, S. Zherebtsov, N. Stepanov, A new refractory Ti-Nb-Hf-Al high entropy alloy strengthened by orthorhombic phase particles, *Int. J. Refract. Metals Hard Mater.* 92 (2020) 105322, <https://doi.org/10.1016/j.ijrmhm.2020.105322>
- [43] A. Lacour-Gogny-Goubert, Z. Huvelin, M. Perrot, D. Boivin, N. Horezan, I. Guillot, P. Vermaut, J.P. Couzine, Effect of Mo, Ta, V and Zr on a duplex bcc+orthorhombic refractory complex concentrated alloy using diffusion couples, *Intermetallics* 124 (2020) 106836, <https://doi.org/10.1016/j.intermet.2020.106836>
- [44] S. Zherebtsov, N. Yurchenko, E. Panina, M. Tikhonovsky, N. Stepanov, Gum-like mechanical behavior of a partially ordered Al₅Nb₂Ti₄MoV₅Zr₂₆ high entropy alloy, *Intermetallics* 116 (2020) 106652, <https://doi.org/10.1016/j.intermet.2019.106652>
- [45] S. Zherebtsov, N. Yurchenko, E. Panina, A. Tojibaev, M. Tikhonovsky, G. Salishchev, N. Stepanov, Microband-induced plasticity in a Ti-rich high-entropy alloy, *J. Alloy. Compd.* 842 (2020) 155868, <https://doi.org/10.1016/j.jallcom.2020.155868>
- [46] J.W. Zhang, S.Q. Li, D.X. Zou, W.Q. Ma, Z.Y. Zhong, Processing and microstructure control of (α +B₂+O) alloy sheet in Ti-Al-Nb system, *Intermetallics* 8 (2000) 699–702, [https://doi.org/10.1016/S0966-9795\(99\)00148-X](https://doi.org/10.1016/S0966-9795(99)00148-X)
- [47] N.Y. Yurchenko, N.D. Stepanov, S. V. Zherebtsov, M.A. Tikhonovsky, G.A. Salishchev, Structure and Mechanical Properties of B2 Ordered Refractory AlNbTiZr x ($x = 0-1.5$) High-entropy Alloys, 2017. (<https://doi.org/10.1016/j.msea.2017.08.019>).
- [48] M.C. Tropicovsky, J.R. Morris, P.R.C. Kent, A.R. Lupini, G.M. Stocks, Criteria for predicting the formation of single-phase high-entropy alloys, *Phys. Rev. X* 5 (2015) 11041, <https://doi.org/10.1103/PhysRevX.5.011041>
- [49] K.N. Wertz, J.D. Miller, O.N. Senkov, Toward multi-principal component alloy discovery: assessment of CALPHAD thermodynamic databases for prediction of novel ternary alloy systems, *J. Mater. Res.* 33 (2018) 3204–3217, <https://doi.org/10.1557/jmr.2018.61>
- [50] K. Muraleedharan, T.K. Nandy, D. Banerjee, S. Lele, Phase stability and ordering behaviour of the O phase in TiAlNb alloys, *Intermetallics* 3 (1995) 187–199, [https://doi.org/10.1016/0966-9795\(95\)98930-7](https://doi.org/10.1016/0966-9795(95)98930-7)
- [51] D. Banerjee, The intermetallic Ti₂AlNb, *Prog. Mater. Sci.* 42 (1997) 135–158, [https://doi.org/10.1016/S0079-6425\(97\)00012-1](https://doi.org/10.1016/S0079-6425(97)00012-1)
- [52] C.J. Boehlert, B.S. Majumdar, V. Seetharaman, D.B. Miracle, Part I. The microstructural evolution in Ti-Al-Nb O + Bcc orthorhombic alloys, *Metall. Mater. Trans. A* 30 (1999) 2305–2323.
- [53] K. Muraleedharan, A.K. Gogia, T.K. Nandy, D. Banerjee, S. Lele, Transformations in a Ti-24Al-15Nb alloy: Part I. Phase equilibria and microstructure, *Metall. Trans. A* 23 (1992) 401–415, <https://doi.org/10.1007/BF02801158>
- [54] W. Chen, Q.H. Tang, H. Wang, Y.C. Xie, X.H. Yan, P.Q. Dai, Microstructure and mechanical properties of a novel refractory AlNbTiZr high-entropy alloy, *Mater. Sci. Technol.* 34 (2018) 1309–1315, <https://doi.org/10.1080/02670836.2018.1446267>
- [55] T. Gladman, Precipitation hardening in metals, *Mater. Sci. Technol.* 15 (1999) 30–36, <https://doi.org/10.1179/026708399773002782>
- [56] B. Chen, J. Shen, X. Ye, L. Jia, S. Li, J. Umeda, M. Takahashi, K. Kondoh, Length effect of carbon nanotubes on the strengthening mechanisms in metal matrix composites, *Acta Mater.* 140 (2017) 317–325, <https://doi.org/10.1016/j.actamat.2017.08.048>
- [57] I. Toda-Caraballo, P.E.J. Rivera-Díaz-Del-Castillo, Modelling solid solution hardening in high entropy alloys, *Acta Mater.* 85 (2015) 14–23, <https://doi.org/10.1016/j.actamat.2014.11.014>
- [58] I. Toda-Caraballo, A general formulation for solid solution hardening effect in multicomponent alloys, *Scr. Mater.* 127 (2017) 113–117, <https://doi.org/10.1016/j.scriptamat.2016.09.009>
- [59] C. Varvenne, A. Luque, W.A. Curtin, Theory of strengthening in fcc high entropy alloys, *Acta Mater.* 118 (2016) 164–176, <https://doi.org/10.1016/j.actamat.2016.07.040>
- [60] C. Varvenne, G.P.M. Leyson, M. Ghazisaeidi, W.A. Curtin, Solute strengthening in random alloys, *Acta Mater.* 124 (2017) 660–683, <https://doi.org/10.1016/j.actamat.2016.09.046>
- [61] R.R. Eleti, N. Stepanov, N. Yurchenko, D. Klimenko, S. Zherebtsov, Plastic deformation of solid-solution strengthened Hf-Nb-Ta-Ti-Zr body-centered cubic medium/high-entropy alloys, *Scr. Mater.* 200 (2021) 113927, <https://doi.org/10.1016/j.scriptamat.2021.113927>